Electronic Supplementary Material (ESI) for RSC Advances.

Simply packaging Ni nanoparticles inside SBA-15 channels by co-impregnation for dry reforming of methane

Songbai Qiu, Qiao Zhang, Wei Lv, Tiejun Wang*, Qi Zhang and Longlong Ma

Key Laboratory of Renewable Energy, Guangdong Key Laboratory of New and Renewable Energy Research and Development, Guangzhou Institute of Energy Conversion, Chinese Academy of Sciences, Guangzhou 510640, PR China Email: wangtj@ms.giec.ac.cn. Fax: +86 20 87057789

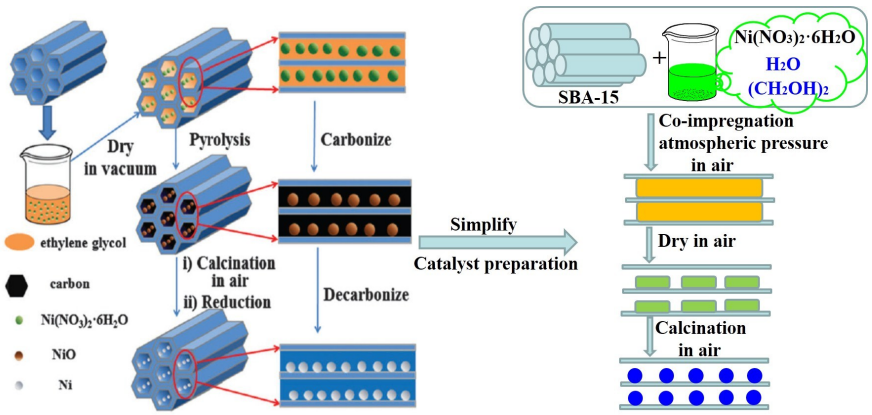

Supplementary SFig. 1 Schematic illustration of the different preparation process for the Ni@SBA-15 catalyst using EG.

As shown in the supplementary SFig. 1, we utilized the EG aqueous solution to replace pure solvent of EG as reported in literature [1], and simplified this preparation route and developed one more simple and practical preparation method of co-impregnation for preparing the Ni@SBA-15 catalyst. Comparing with the conventional wetness impregnation, the only difference of co-impregnation is that there is need to add proper EG into the nickel nitrate aqueous solution, and the other preparations have the same procedures. Moreover, the simplified preparation route could avoid not only the drying in vacuum but also the carbonization under an inert atmosphere. The EG in the nickel nitrate aqueous solution could assist the Ni precursor in entering into the SBA-15 channels easily by capillary force, and

as solvent continually evaporating, the additive EG was adsorbed onto the internal surface of mesoporous channels, which inhibited redistribution and agglomeration of impregnated solution upon drying of the support.

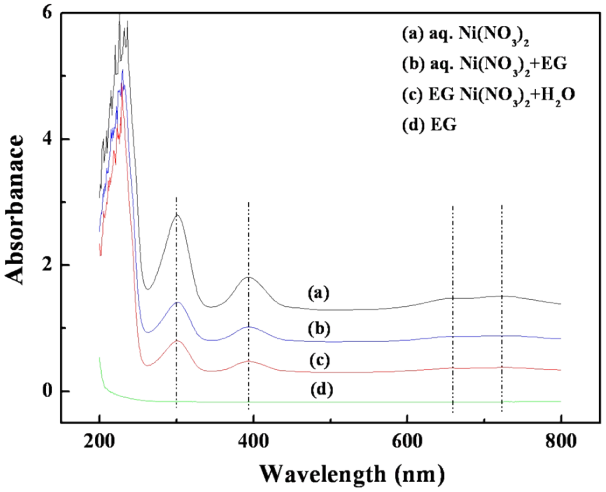

Supplementary SFig. 2 The UV absorption spectrum of samples (a) 0.57mol/L $Ni(NO_3)_2$ in aqueous solution; (b) 0.057mol/L $Ni(NO_3)_2$ and 0.17 mol/L EG in aqueous solution; (c) 0.057mol/L $Ni(NO_3)_2$ and 0.17 mol/L H_2O in EG solution; (d) pure EG.

Firstly, we utilized the UV–vis spectra to experimentally observe the complexing and interacting between Ni^{2+} ions and ethylene glycol (EG) during co-impregnating (supplementary SFig. 2). So as to reveal coordination effect between Ni^{2+} ions and EG, we studied the UV–vis spectra of the nickel nitrate solutions in the absence of MCM-41 support. It was noteworthy that the main peak positions at the 393 nm (3A2g to 3T1g (P) transition) showed no obvious shift. This suggests that adding EG to the impregnating solutions of nickle nitrate did not significantly modify nickle local coordination. Therefore, it is difficult to produce new coordination compound under the impregnation conditions (This data has not been added into the revised manuscript for provision of article length). The UV absorption spectrum of NO_3^- ion in aqueous solution was well known to contain two bands: a very strong one at $\approx$ 230 nm (assigned to $\pi^* \leftarrow \pi$ transition) and a weaker one near 300 nm (assigned to $\pi^* \leftarrow$n transition) [2-3]. As a first-row transition metal, aqueous Ni^{2+} displays a typical octahedral structure with six water ligands in the first coordination shell [4]. Spectra for the nickel nitrate system showed two major absorption bands in the 300–800 nm range. The peak at 722 nm and a shoulder at 658 nm was split from the d-d transition bands (3A2g to 3T1g) due to spin-orbit coupling that mixing the 3T1g(F) and 1Eg states.

Commonly, the infiltration solutions into the pores of the support could be explained by the capillary pressure using the Young−Laplace equation [5]:

$$\Delta p = (2\gamma_{lv}/r_p)\cos\theta$$

Where Δp is the capillary pressure difference, r_p is a pore with radius, γ_{lv} is the liquid surface tension, and θ is the wetting angle between the solid and the liquid. From this equation, it is clear that the pressure difference depends inversely on the pore size, so that the impregnation solution is preferentially sucked up by the smallest pores, and generally fast fills the pores. But many experimental tests may not fully support the theoretical predictions due to the complexity of the actual preparation process and the support's natural instincts. Firstly, the MCM-41 and SBA-15 supports are not fully hydrophilic, which are attributed to the relatively low hydroxyl density of mesoporous silica, resulting in incomplete wetting [6]. Although pore filling occurs rapidly, inhomogeneous filling during impregnation is inevitable, and the wetting and infiltration degree into the mesoporous channels appear particularly important. In addition, the thermal treatment such as drying after impregnation may cause the redistribution of the precursor and inhomogeneous distributions inside the catalyst supports as the solvent constantly evaporates. In this case, it suggests that the thermal treatment after impregnation plays a more significant role in the distribution of the precursor.

As the solvent is removed during drying, the concentration of the precursor will rise, and the properties of impregnation solutions changes a lot, which is very important for high dispersions of the active phase after full drying. Therefore, upon gradual removal of the solvent, the surface tension and viscosity of impregnation solutions with different water content were measured in Table 1 and Table 2 in the manuscript. It should be noted that addition of EG into the nickel nitrate aqueous solution has been shown to decrease the surface tension of impregnation solutions, and there was a gradual decrease upon evaporation of the solvents. Interestingly, the presence of EG could work as a surfactant; as the solvent was gradually removed during drying, the decreased surface tension of impregnation solutions favored better wetting of the support, and accelerated diffusion and infusion into the deeper mesoporous channels of the catalyst support. Meanwhile, we have measured the effect of solvent removal on the viscosity. The results were shown in Table 2 in the manuscript. The figure showed that the viscosity rose slowly during the initial of drying, and then it exhibited a rapid increase of the viscosity of the impregnation solutions, especially late in drying. At first, drying mainly occurred on the external surface of the drying support. As drying proceeded, a continuous liquid existed throughout the external surface and the mesoporous channels of the SBA-15 support; such that the concentrated solvent with the lower surface tension could be diffused deeply and transported toward the internal surface of the mesoporous channels via capillary forces; the enhanced viscosity could lead to a strong interaction with the support internal surface and inhibited redistribution of the impregnation solution during drying, thus favoring a uniform distribution of the active component in the mesoporous channels. But on the contrary, the precursor has a weak interaction with support without EG, and the concentrated solvent sucked up by the mesoporous pores could be back-diffused and migrated toward the external surface of the mesoporous channels, resulting in a concentration buildup on the external rim of the support. As a consequence, inhomogeneous distributions of the precursor appeared.

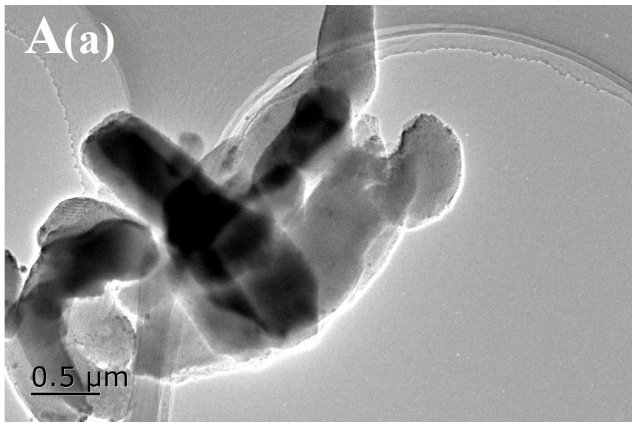

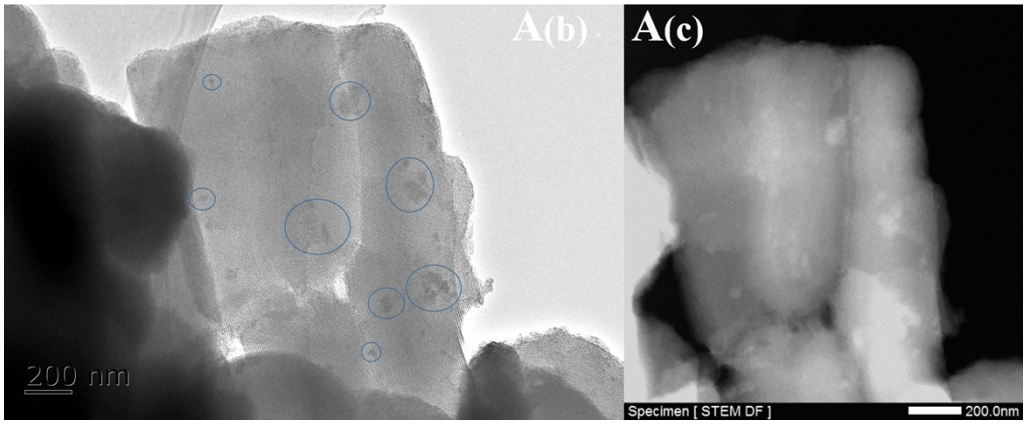

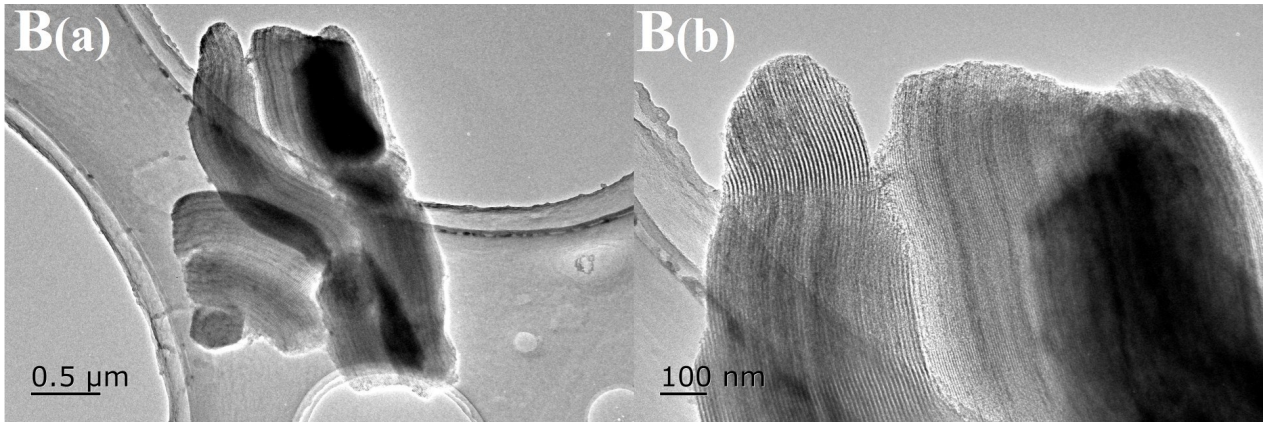

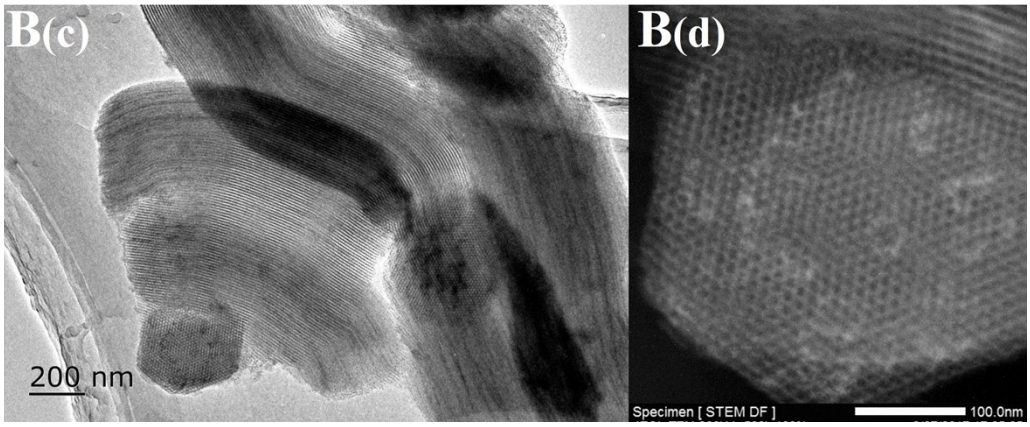

Supplementary SFig. 3 TEM images of the Ni-based catalysts after drying at 100 ºC without calcination: (A)

Ni/SBA-15 and (B) Ni@SBA-15.

More visual measurements have also provided evidence on the above views by the TEM images of the Ni-based catalysts after drying at 100 ^{o}C without calcination. Supplementary SFig. 3 has shown that inhomogeneous distributions of the precursor has formed after drying even if there was no subsequent calcination and reduction, while use of EG as a co-impregnation solvent resulted in specially homogeneous distributions and no aggregates were found, which was attributed to the lower surface tension and higher viscosity of the concentrated impregnation solution during drying. Furthermore, supplementary SFig. 3B(d) TEM images displayed that the SBA-15 pores were not completely filled with the precursor, suggesting that the SBA-15 support was not fully hydrophilic due to the relatively low hydroxyl density of mesoporous silica, resulting in incomplete wetting.

Supplementary SFig. 4 showed the TG-DSC curves of decomposition for samples after drying at 100 ^{o}C and their in-situ FT-IR spectra of decomposition products. The DSC curves showed a broad endothermic peak below 160 ^{o}C corresponding to the removal of the absorbed water. The sample co-impregnated with EG represented one acceleratory stage in the temperature range of 160–250 °C in which the weight loss increased quickly to 16.2%, which was attributed to the decomposition of EG and partial nickel nitrate. In comparison, it was noted that there were two type peaks at 285 ^{o}C, relating to the exothermal process and the endothermal process. The actual mass losses of the last degression stage occurred between 250 and 400 ^{o}C were 7.7% and 2.8% for Ni/SBA-15 without EG and Ni@SBA-15 with EG, respectively. Weightlessness slightly occurred above 400 °C, which means that the decomposition reaction was almost finished. The corresponding in-situ FT-IR spectra of decomposition products also confirmed the TG-DSC results mentioned above. There were two types of infrared absorption peaks observed, corresponding to NO_2 and CO_2. The bands at 1595 cm^{-1} and 1629 cm^{-1} was associated to NO_2. Besides, the evident sharp bands at 669 cm^{-1}, 2310 cm^{-1} and 2358 cm^{-1} were attributed to the absorption of CO_2. However, for the Ni/SBA-15 sample, an additional bands of CO_2 was evidently observed even if there was no EG, which could be assigned to CO_2 adsorbed on the sample in air and outgassed at high temperature during temperature programmed decomposition. The broad band from 3000 cm^{-1} to 3500 cm^{-1} was attributed to approach the infrared detection limit of the detector (TENSOR27 FTIR) or overlap the absorption of H_2O. For the Ni@SBA-15 sample using co-impregnation with EG, the in-situ FT-IR spectra of decomposition products also confirmed that there was one overlapping procedure between the oxygenolysis of EG and the decomposition of nickel nitrate. Based on these measurements, it was considered that addition of EG during co-impregnated changed the thermal decomposition behavior of the samples, i.e., the heat released from thermal decomposing of the adsorbed EG on SBA-15 surface was quickly absorbed by impregnated nickel nitrate to supply energy for decomposition, which led to increasing of the nickel nitrate decomposition in low temperature rang (at 221

°C). These maybe efficiently prevent further aggregation of the precursor, contributing to improving NiO dispersion inside the SBA-15 channels.

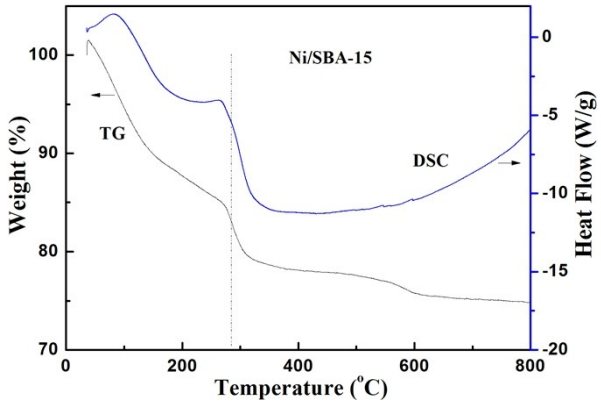

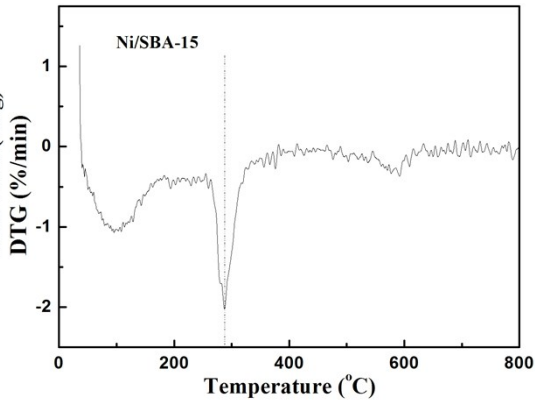

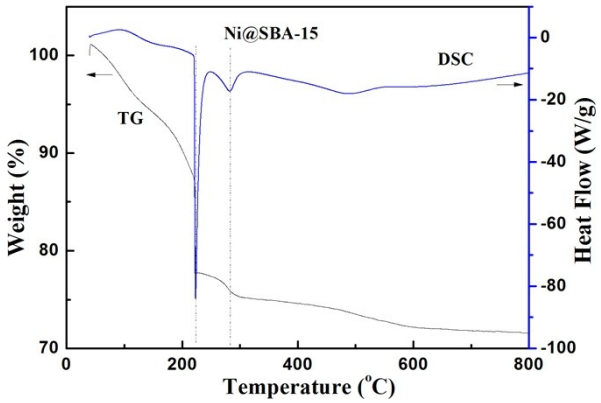

(a) Ni/SBA-15 after drying

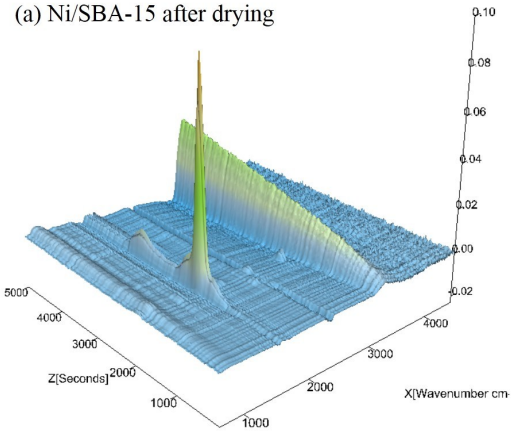

(b) Ni@SBA-15 after drying

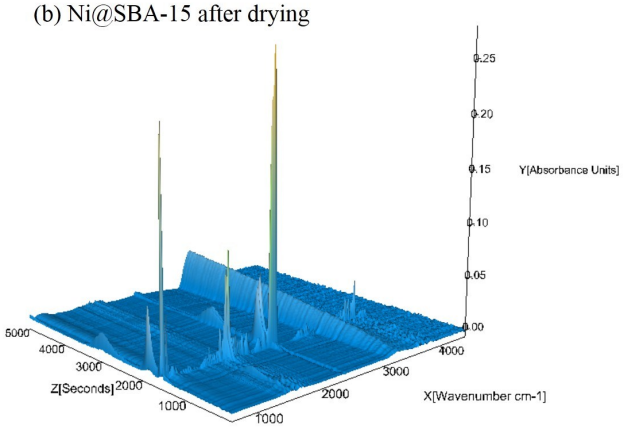

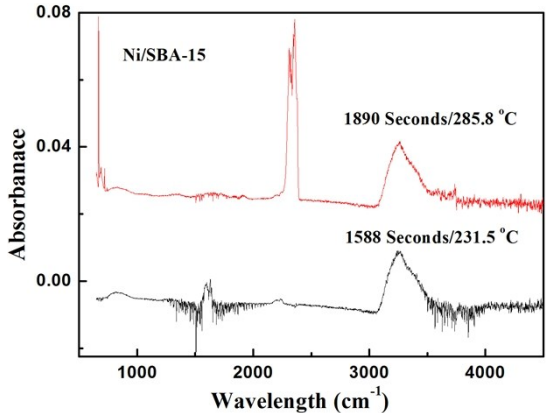

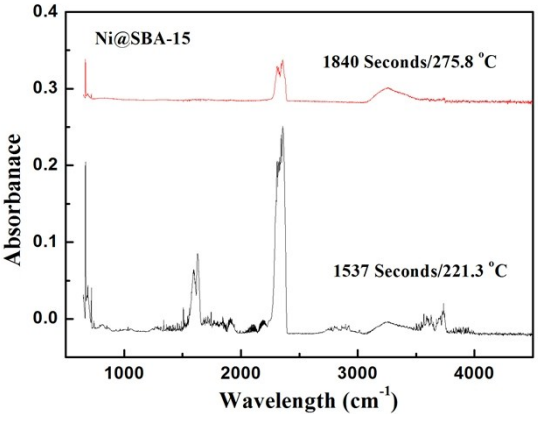

Supplementary SFig. 4 TG-DSC curves of decomposition for samples after drying and their in-situ FT-IR spectra of decomposition products.

As shown in Table 3 in the manuscript, the Ni metal dispersion and crystallite sizes of the different Ni-based catalysts were measured using hydrogen-temperature program desorption technique (H_2-TPD) on a Micromeritics Autochem apparatus (model 2910). It was clearly proved that the co-impregnation with EG efficiently enhanced the dispersion of supported nickel on the SBA-15 support. The particle size of two catalysts was also determined by hydrogen chemisorption, as 5.3 nm for Ni@SBA-15 and 12.9 nm for Ni/SBA-15 respectively (assuming spherical metal crystallites), which was in good agreement with the XRD and TEM analysis. The test details: for each test, the sample weight was about 100 mg. The catalysts should be pre-reduced using 10% H_2/Ar at 700 ^oC for 1 h. After cooling, the samples were purged under flowing Ar to remove physical absorbed and/or weakly bound species at 50 ^oC. The hydrogen desorption was monitored by the thermal conductivity detector (TCD) at a temperature ramp 10 ^oC/min up to 700 ^oC in Ar. The dispersion and crystallite sizes were determined from the amount of H_2 desorption in the H_2-TPD, in which the H_2 adsorption was assumed as $Ni_{surface}/H = 1$ and the supported metal was fully reduced. The concrete design method and calculation formula was obtained according to the reference [7].

Surface areas and pore volumes and diameters of the samples were calculated using standard BET and BJH theory, respectively. The N_2 adsorption/desorption isotherms of the samples and the pore size distribution were presented Fig. 1 in the manuscript. These isotherms are typical of a reversible type IV with a hysteretic loop based on the IUPAC classification scheme for mesoporous materials, with a narrow pore size distribution of the cylindrical pores, in well agreement with XRD at low angle and TEM observations. However, new steps were clearly present on the desorption branch of the Ni@SBA-15 sample, which generated delays in the closing of the hysteresis loops at approximately 0.4-0.6. This indicates that a new porous system was present in tubular SBA-15, according to the capillary condensation model, which was previously indicated as possible in ink-bottle mesopores [8]. At the same time, two porous systems were obviously noted on the Ni@SBA-15 sample, as shown in the pore size distribution (Fig. 1B in the manuscript). Primary mesopores with an average diameter was 5.66nm, and that of one new mesopores was 3.38nm. These two porous systems were the direct evidence of the blockage of primary mesopores with confined NiO nanoparticles, which was in line with the above measurements. Therefore, this new type of mesopores arose as a result of the partial blocking of the SBA-15 channels with confined NiO nanoparticles. The test details: the raw material of SBA-15 support was commercially purchased from Nanjing XFNANO Materials Tech Co., Ltd. (Nanjing, China). Prior to impregnation, the SBA-15 support should be calcined in air at 550 ^oC for 4h to eliminate the residual organic effect. The BET specific surface area of catalysts was determined by N_2 isothermal adsorption using QUADRASORB SI analyzer equipped with

QuadraWin software system. Special surface areas and pore volumes and diameters of the samples were calculated using standard BET and BJH theory respectively. For each run, the samples were outgassed at 250 °C for 11 h.

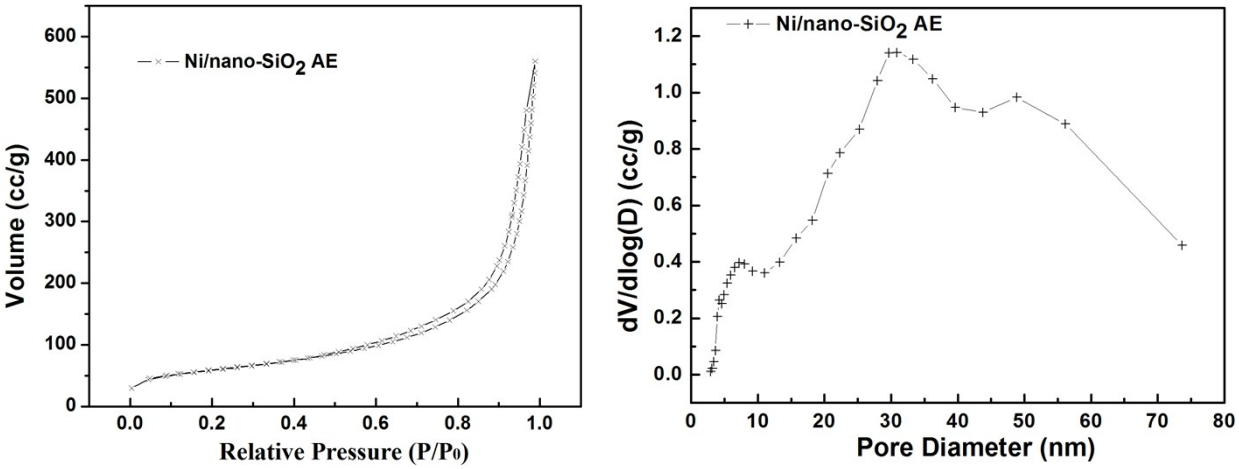

Supplementary SFig. 5 (A) Nitrogen adsorption isotherms and (B) pore size distribution of the Ni/nano-SiO_2 AE sample.

Supplementary STable 1 Textural properties of the Ni/nano-SiO_2 AE sample.

Samples	Impregnation solvent	S_{BET} (m^2/g)[b]	Pore volume (cm^3/g)[b]	Most probable pore diameter (nm)[b]	Dispersion (%)[d]	Ni particle size (nm)[a]
Ni/nano-SiO_2 AE[c]	ammonia+water	207	0.89	30.20	17.4	4.8 (5.8[d])

[a] After reduction at 700 °C for 1 h, Ni particle size was calculated by Scherrer's equation, the Bragg angle of 2θ using 44.5°.

[b] Surface areas and pore volumes and diameters of the samples were calculated using standard BET and BJH theory respectively.

[c] The sample was prepared by an ammonia evaporation method (the mole ratio of ammonia to nickel was 10:1). The metal loading was 10.79 wt.% by ICP-AES.

[d] The dispersion and crystallite sizes of metallic Ni were determined from the amount of H_2 desorption in the H_2-TPD at 50 °C, in which the H_2 adsorption was assumed as $Ni_{surface}/H = 1$ and the supported metal was fully reduced.

In order to compare confinement and dispersion impacts on the catalytic performance, we prepared the high dispersed Ni catalyst supported on nano-SiO_2 without typical mesoporous structures. Nano-SiO_2 (average particle size 20 nm) was supplied by Nanjing XFNANO Materials Tech Co., Ltd. (Nanjing, China) as support materials. The Ni supported on nano-SiO_2 was prepared by an ammonia evaporation method (the mole ratio of ammonia to nickel was

10:1). The other preparation process was the same with that of the manuscript. The obtained catalysts via the ammonia evaporation method were denoted as Ni/nano-SiO_2 AE. The N_2 adsorption/desorption isotherms of the samples and the pore size distribution were presented supplementary SFig. 5. The corresponding textural parameters were presented in supplementary Table 1. The Ni/nano-SiO_2 AE sample did not exhibit type mesoporous structure. It was very difficult to distinguish the predominance distribution of mesoporous channels. The mesoporous distribution in the range of 3nm-70nm was attributed to the disorder stacking of amorphous SiO_2 nanoparticles. The aggregation of nano-SiO_2 particles formed loose and porous structure with no strong texture.

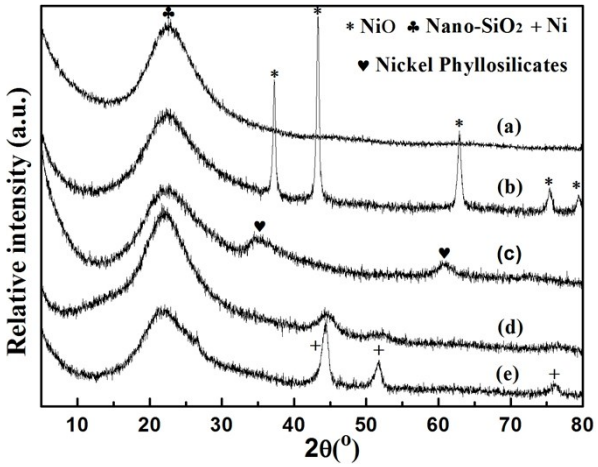

Supplementary SFig. 6 XRD patterns for the Ni-based catalysts supported on nano-SiO_2: (a) nano-SiO_2; (b) Ni/nano-SiO_2 prepared by conventional incipient wetness impregnation; (c) Ni/nano-SiO_2 AE prepared by an ammonia evaporation method; (d) Ni/nano-SiO2 AE after reduction and (e) Ni/nano-SiO2 AE after the stability test.

The XRD patterns of the Ni/nano-SiO_2 AE sample before and after testing were also shown in supplementary SFig. 6. Using conventional incipient wetness impregnation, five intensive diffraction peaks of NiO were detected after calcination. In contrast, the Ni/nano-SiO_2 AE sample showed two weak and diffuse diffraction peaks at 2Θ = 34.1° and 60.5° corresponding to nickel phyllosilicate, confirming that nickel species were very small and highly dispersed on the nano-SiO_2 support. As shown in supplementary SFig. 9A, the TEM images further present two kinds of microstructures in the Ni catalysts, bits of spherical particles and dominative lamellar structures consisting of claylike lines, indicating the presence of both NiO and nickel phyllosilicate. After H_2 reduction at 700 °C for 1 h, the new diffraction peaks of Ni clearly emerged in supplementary SFig. 6d. The average particle size of spherical Ni nanoparticles was 4.8 nm, according to calculation by Scherrer's equation at 2θ angle of 43.3°. As shown in supplementary STable 1, the Ni metal dispersion and crystallite sizes of Ni/nano-SiO_2 AE were measured using hydrogen-temperature program desorption technique (H_2-TPD). The characterization results

exhibited that the highly dispersed and uniformly distributed Ni nanoparticles could be obtained by the ammonia evaporation method. The presence of Ni phyllosilicate was crucial to obtain Ni nanoparticles with the dispersion of 17.4% after reduction by H_2, which exhibited an analogous narrow size distribution with in the sample prepared by co-impregnation with EG. The particle size was about 5.8 nm for Ni/nano-SiO_2 AE, which was similar with that of Ni@SBA-15.

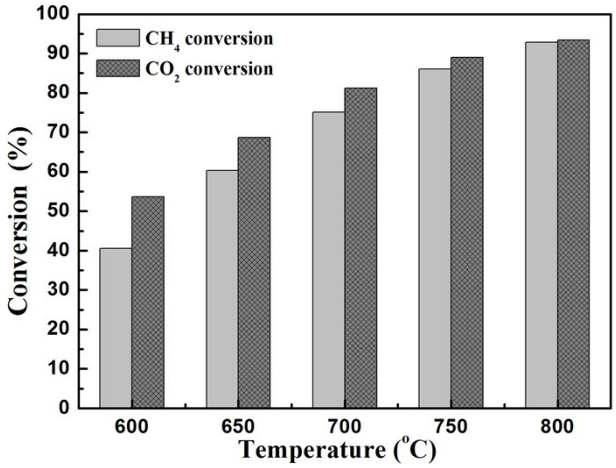

Supplementary SFig. 7 The conversions of CH_4 and CO_2 in the DRM reaction at different temperatures for Ni/nano-SiO_2 AE; Reaction conditions: P = 1 atm, CO_2/CH_4 = 1:1, GHSV = 36000 $cm^3\ g^{-1}\ h^{-1}$.

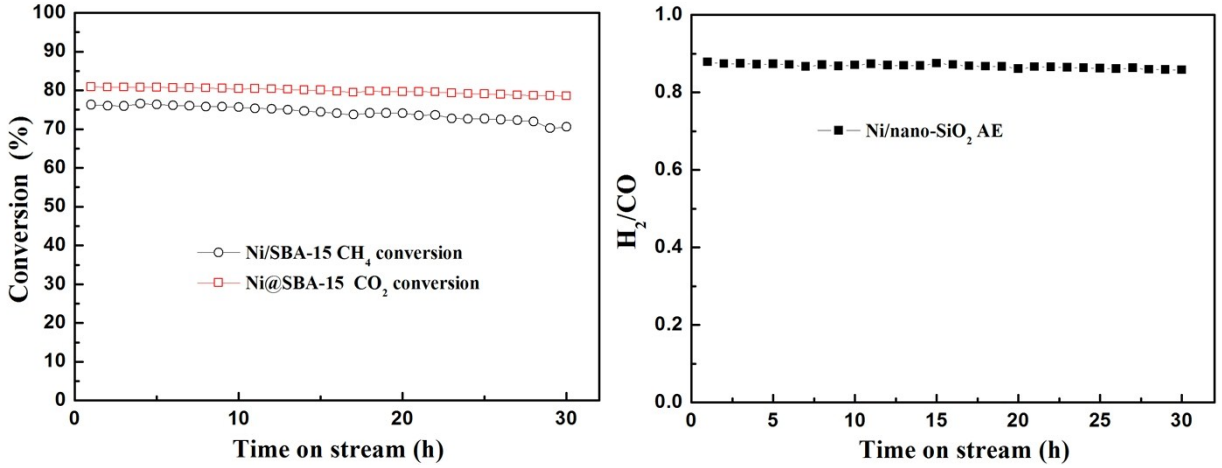

Supplementary SFig. 8 The catalytic stability of Ni/nano-SiO_2 AE in the DRM reaction; Reaction conditions: P = 1 atm, T = 700 °C, CO_2/CH_4 = 1:1, GHSV = 36000 $cm^3\ g^{-1}\ h^{-1}$.

After reduction, the samples of Ni@SBA-15 and Ni/nano-SiO_2 AE displayed the approximate crystal sizes and dispersion of metallic Ni nanoparticles; in addition, the Ni/nano-SiO_2 AE sample had no typical mesoporous structures and the Ni nanoparticles were highly dispersed on the external surface of nano-SiO_2 support; thus, it was contributed to compare confinement and dispersion impacts on the catalytic performance. The Ni/nano-SiO_2 AE catalyst was further applied in the DRM reaction for comparing the catalytic activity and stability. As depicted

in supplementary SFig. 7, the conversions of CH_4 and CO_2 both increased with the increase of reaction temperature from 600 ^oC to 800 ^oC under atmospheric pressure. The Ni/nano-SiO_2 AE catalyst expressed the similar activity with that of the Ni@SBA-15catalyst, and it showed better catalytic activity by comparing with the Ni/SBA-15 catalyst obtained by conventional impregnation. At 800 ^oC, for the Ni/nano-SiO_2 AE catalyst, the CH_4 conversion was increased to 92.9% and the CO_2 conversion reached 93.4%. Therefore, the higher activity of the Ni@SBA-15 catalyst and the Ni/nano-SiO_2 AE catalyst should be ascribed to smaller particle size and higher dispersion of Ni species supported on supports.

The long-term catalytic stability test of the Ni/nano-SiO_2 AE catalyst were performed at 700 ^oC for 30 h. As displayed in supplementary SFig. 8, the conversion of CH_4 and CO_2 both gradually decreased little by little with time on stream. Conversely, the Ni@SBA-15 catalyst remained stable with no apparent deactivation observed in the harsh DRM reaction. It was well known that the deactivation of Ni-based catalysts was caused by sintering of Ni species and carbon deposition. In order to explore the reason of deactivation, XRD profiles, TG and DSC profiles and TEM imagines of the used Ni-based catalysts after a long-term stability test were investigated in supplementary Fig. S6, supplementary SFig. 9 and supplementary SFig. 10. For the used Ni/nano-SiO_2 AE catalyst, the XRD profiles indicated that the peaks of Ni obviously exhibited more stronger and sharper, suggesting that the Ni nanoparticles aggregated into even larger clusters on the nano-SiO_2 surface, which was further confirmed by the TEM images. After reaction, the average diameter of Ni nanoparticles grew up from 4.8 nm to 8.6 nm, according to calculation by the Scherrer formula. Due to the absence of the confinement effect of mesoporous channels and strong metal-support interactions, the Ni nanoparticles supported on the nano-SiO_2 surface were easily suffered from the serious sintering during the harsh DRM reaction. As depicted in supplementary SFig. 10, the carbon deposition over the used Ni/nano-SiO_2 AE catalyst was quantified by TG-DSC measurements. The weight loss of the used Ni/nano-SiO_2 AE catalyst at high temperatures (500-750 ^oC) was 2.6%. The Ni/nano-SiO_2 AE catalyst presented the least carbon deposition, which was consistent with the TEM observation. This could be explained by that the small Ni nanoparticles with high dispersion facilitated to improve the resistance of coking. Based on the results above, it revealed that sintering of Ni species was mainly responsible for activity loss of the Ni/nano-SiO_2 AE catalyst.

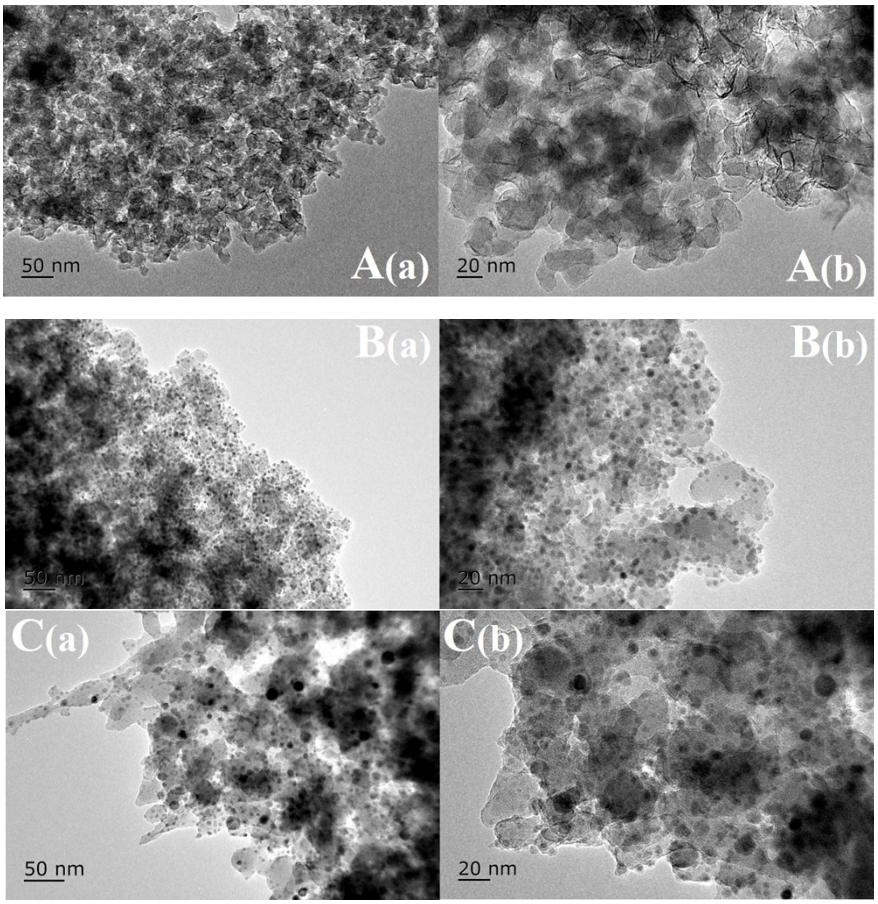

Supplementary SFig. 9 TEM images of Ni/nano-SiO_2 AE: (A) after calcination; (B) after reduction and (C) after the stability test in the DRM reaction.

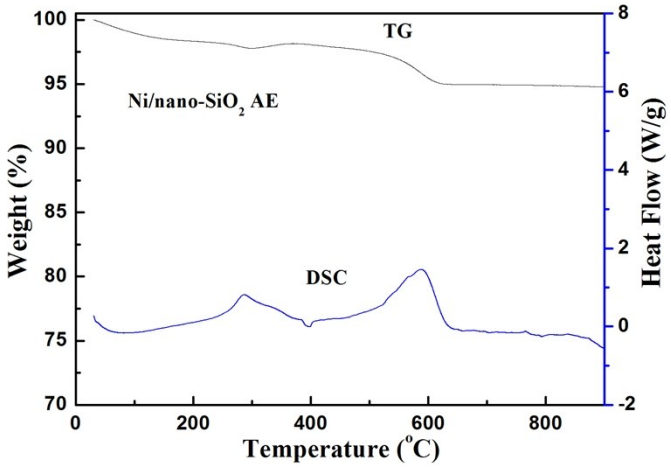

Supplementary SFig. 10 TG and DSC profiles of Ni/nano-SiO_2 AE after the stability test in the DRM reaction.

So as to compare the catalytic activity in the DRM reaction, the turnover frequency (TOF) values of CH_4 for the three samples calculated in supplementary STable 2. Obviously, the Ni@SBA-15 prepared by co-impregnation showed the best catalytic activity. In order to estimate the sintering ability of Ni-based catalysts, the catalysts were maintained at 800 ^oC for 1 h after the heating stage and then the temperature was cooled down. The Ni@SBA-15 catalyst almost kept all the initial activity while the Ni/SBA-15 catalyst suffered from the severe deactivation and lost

about 75.0% of initial activity at 600 °C. It was noted that the Ni/nano-SiO_2 AE still retained 89.0% of the initial activity at 600 °C in spite of sintering. Thus, the activity of the Ni/SBA-15 catalyst declined sharply mainly due to sintering of Ni species and carbon deposition.

Supplementary STable 2 The TOF values of CH4 for the Ni-based catalysts during the DRM reaction.

Samples	Ni loading (wt%)[a]	TOF (h^{-1})[b]				
		600 °C	650 °C	700 °C	750 °C	800 °C
Ni/SBA-15	9.62	441.2(103.0)	473.3(251.2)	580.4(464.1)	714.9(685.1)	862.1(853.8)
Ni@SBA-15	8.70	492.8(487.9)	662.8(654.2)	819.0(820.3)	935.9(937.6)	1007.7(1007.8)
Ni/nano-SiO_2 AE	10.79	354.6(315.6)	527.6(493.1)	656.9(650.2)	752.7(751.8)	811.9(811.1)

[a] The metal loadings were determined by ICP-AES.

[b] The TOF values in brackets were tested in the cooling stage, the others were tested in the heating stage. The activity of catalysts was tested in the range of 600-800 °C at a 50 °C increment. When the temperature rose to the desired level, maintained for 30 min before the test. The temperature was maintained at 800 °C for 1 h before the temperature cool down. Reaction conditions: P = 1 atm, CO_2/CH_4 = 1:1, GHSV = 36000 $cm^3\ g^{-1}\ h^{-1}$.

References used in supporting materials:

[1] Ting Xie, Liyi Shi, Jianping Zhang and Dengsong Zhang. Immobilizing Ni nanoparticles to mesoporous silica with size and location control via a polyol-assisted route for coking- and sintering-resistant dry reforming of methane. Chem. Commun., 2014, 50, 7250-7253.

[2] Weihua Liu, Artas Migdisov and Anthony Williams-Jones. The stability of aqueous nickel (II) chloride complexes in hydrothermal solutions: Results of UV–Visible spectroscopic experiments. Geochimica et Cosmochimica Acta, 94, 2012, 276-290.

[3] Vlatka Gvozdić, Vladislav Tomišić, Vjekoslav Butorac and Vladimir Simeon. Association of Nitrate Ion with Metal Cations in Aqueous Solution: a UV-Vis Spectrometric and Factor-Analytical Study. Croat. Chem. Acta, 82, 2009, 553-559.

[4] Christopher J. Thompson, John Husband, Fernando Aguirre and Ricardo B. Metz. Photo-dissociation Dynamics of Hydrated Ni^{2+} Clusters: $Ni^{2+}(H_2O)n$ (n = 4-7), J. Phys. Chem. A, 104, 2000, 8155-8159.

[5] Peter Munnik, Petra E. de Jongh and Krijn P. de Jong. Recent Developments in the Synthesis of Supported Catalysts. Chem. Rev., 115, 2015, 6687-6718.

[6] Sietsma, J. R. A.; Meeldijk, J. D.; Versluijs-Helder, M.; Broersma, A.; van Dillen, J. A.; de Jongh, P. E. and de Jong, K. P. Ordered Mesoporous Silica to Study the Preparation of Ni/SiO_2 ex Nitrate Catalysts: Impregnation, Drying, and Thermal Treatments. Chem. Mater., 20(9), 2008, 2921-2931.

[7] Subramani Velu and Santosh K. Gangwal. Synthesis of alumina supported nickel nanoparticle catalysts and evaluation of nickel metal dispersions by temperature programmed desorption. Solid State Ionics 177, 2006, 803-811.

[8] Adrian Ungureanu, Brindusa Dragoi, Alexandru Chirieac, Sebastien Royer, Daniel Duprez and Emil Dumitriu. Synthesis of highly thermostable copper-nickel nanoparticles confined in the channels of ordered mesoporous

SBA-15 silica. J. Mater. Chem., 21, 2011, 12529-12541.